Stability of the Tropical Cyclone Intensity Equilibrium

CHANH KIEU

Department of Earth and Atmospheric Sciences, Indiana University Bloomington, Bloomington, Indiana

QUAN WANG

Department of Earth and Atmospheric Sciences, Indiana University Bloomington, Bloomington, Indiana, and Department of Mathematics, Sichuan University, Sichuan, China

(Manuscript received 27 January 2017, in final form 27 July 2017)

ABSTRACT

A low-order dynamical model that demonstrates the stable property of the tropical cyclone (TC) maximum potential intensity (MPI) equilibrium under the wind-induced surface heat exchange feedback was recently presented by Kieu. In this study, an alternative TC-scale model that allows for the gradient wind imbalance in the planetary boundary layer is proposed to further examine the stability of the MPI equilibrium. Despite different balanced assumptions, it is shown that the new TC-scale model possesses a similar MPI equilibrium with the same asymptotic stability. The structurally stable property of the MPI equilibrium is held for a range of the model parameters, regardless of the model initial conditions or numerical configurations. In addition, an explicit dependence of the MPI on the environmental lapse rate is obtained from the new TC-scale model, which reveals subtle impacts of the tropospheric stratification on TC intensity beyond the traditional MPI framework. The existence and interpretation of two distinct time scales during TC development will be also discussed.

1. Introduction

Modeling and observational studies of the tropical cyclone (TC) development have long documented the existence of a maximum intensity limit that a TC can attain in both idealized and real-data experiments (Rotunno and Emanuel 1987; Bryan and Rotunno 2009; Emanuel 2000; Hakim 2011, 2013; Brown and Hakim 2013). The existence of such a maximum potential intensity (MPI) limit as well as the dependence of the MPI on the large-scale environment well accord with the classical MPI theory by which the TC secondary circulation acts as the legs of a Carnot heat engine (Emanuel 1986, 1988; Garner 2015). Under the neutral slantwise convection condition and the gradient wind balance, Emanuel obtained an explicit expression for the MPI as a function of sea surface temperature and outflow temperature, which allows for quantifying the long-term variation of TC intensity and plays a key role in current TC climate research.

Despite well-documented evidence of the MPI limit in TC development, a less-understood but equally important question is the stability of the MPI equilibrium. Practically, an unstable MPI equilibrium would render the MPI limit meaningless for applications, as the MPI would never be reached. As such, it is of importance to establish the stability of the MPI equilibrium before it can be used to derive a reliable estimation of the TC maximum intensity or quantify the dependence of the MPI on the large-scale environment.

In an attempt to address the stability of the MPI equilibrium from a thermodynamic perspective, Schönemann and Frisius (2012) presented a simplified model that is based on the exchange of saturated entropy between the eyewall and the planetary boundary layer (PBL). In this model, the MPI equilibrium is determined as a constraint at which the exchange of entropy becomes stationary. Because of a complex relationship between the saturated PBL entropy and the mass flux across the absolute angular surfaces within the eyewall region, the stability of the MPI is not explicitly obtained from this model but rather through a range of numerical simulations in which sea surface temperature (SST) and the PBL relative humidity are treated as model parameters. Their analyses of the MPI constraint

Corresponding author: Chanh Kieu, ckieu@indiana.edu

DOI: 10.1175/JAS-D-17-0028.1

showed two stable points: one corresponding to the MPI equilibrium and the other corresponding to a rest state. Despite the demonstrated stability, the asymptotic limit of the MPI equilibrium in Schönemann and Frisius's (2012) model depends sensitively on several time scales for convective relaxation and diabatic cooling, which render their MPI expression different from Emanuel's MPI limit.

Kieu (2015, hereinafter K2015) recently proposed a different low-order model to study the stability of the MPI equilibrium. By employing specific characteristics of TC scales, including the scales of the maximum tangential wind V, the maximum vertical motion in the TC eyewall W, and the maximum warm anomaly at the storm center B, a set of equations representing the dynamics of the TC scales can be obtained [hereinafter referred to as the hurricane-scale dynamical (HSD) model]. Examination of the stability of the HSD model revealed that the MPI equilibrium is asymptotically stable and unique in the phase space of (V, W, B) under the wind-induced surface heat exchange (WISHE) feedback. The inclusion of radiative forcing could modify the basin of the attraction, but all the main properties of the MPI stability remain valid.

The stable MPI equilibrium as captured in K2015's study explains why numerous idealized simulations of TCs are almost ensured to produce a similar equilibrium under the same ambient environment, regardless of the modeling configurations and parameterizations. To some extent, this result is consistent with the stable MPI examined in Schönemann and Frisius (2012) and reflects a deeper theorem for the development of an axisymmetric rotational flow by which any vortex will have to grow and approach an MPI limit, as the MPI limit is the only end fate of the vortex evolution.

While K2015's model could capture important stability of the MPI equilibrium, a caveat to this model is the use of the gradient wind balance to obtain a relationship between the pressure deficit and the tangential wind. Moreover, an absolute neutral stratification is assumed so that the stability analysis can be simplified, which is, however, not fully justified. An apparent issue with the gradient wind assumption in K2015's model is that this balance is not applicable in the PBL, where the strong convergence of radial inflow is important for the amplification of a TC vortex through the advection of the absolute angular momentum (AAM). One could in principle allow for a three-way balance in the PBL by including the frictional contribution to the central pressure deficit as discussed in Kieu et al. (2010) and K2015. However, this approach would not reveal a possible feedback in the PBL whereby a stronger tangential wind will lead to stronger frictional convergence, which in turn spins up the tangential wind further because of the inward AAM advection (Montgomery and Smith 2014; Smith et al. 2015; Smith and Montgomery 2015). In fact, Smith et al. (2015) proposed that the boundary feedback mechanism related to the AAM advection is a main physical process accounting for the amplification of the surface circulation, thus evoking the importance of the PBL gradient wind imbalance in TC development.

In this study, we wish to present a different low-order model within the TC-scale framework to study the MPI equilibrium, which allows for the imbalance of the gradient wind in the PBL. This reexamination of the MPI stability from a different angle will shed some further light into the stability of the maximum intensity that a TC can attain, thereby establishing the stable property of Emanuel's MPI solution. The rest of the paper is organized as follows: In the next section, a formulation for a new TC-scale model based on the gradient wind imbalance will be presented. Section 3 discusses in details the stability analysis, and some concluding remarks will be presented in the final section.

2. TC-scale dynamic model

Because of its succinct form and completeness in representing systems with strong rotational flows, we start our analyses with the system of anelastic equations in the pseudoheight coordinates as follows (e.g., Ogura and Phillips 1962; Wilhelmson and Ogura 1972; Willoughby 1979):

$$u_t + uu_r + \frac{v}{r}u_\varphi + wu_z - \frac{v^2}{r} = -\phi_r + fv + F_u, \tag{1}$$

$$v_t + uv_r + \frac{v}{r}v_\varphi + wv_z + \frac{uv}{r} = -\frac{1}{r}\phi_\varphi - fu + F_v, \tag{2}$$

$$w_t + uw_r + \frac{v}{r}w_\varphi + ww_z = -\phi_z + b + F_w, \tag{3}$$

$$\frac{1}{r}(ur)_r + \frac{1}{r}v_\varphi + w_z - \frac{w}{H} = 0, \tag{4}$$

$$b_t + ub_r + \frac{v}{r}b_\varphi + Sw = Q, \tag{5}$$

where the pseudoheight $z \equiv -H\ln(p/p_s)$, with H the scale height of the atmosphere and p_s the surface pressure; u, v, and w are wind components in the radial, azimuthal, and vertical directions in the cylindrical coordinate (r, φ, z), respectively; ϕ is the geopotential height perturbation relative to a reference value $\overline{\phi}(z)$; $b \equiv gT'/\overline{T}(z)$ is the buoyancy variable relative to the reference temperature $\overline{T}(z)$; f is the Coriolis parameter; $F_{u,v,w}$ denote the frictional forces in the PBL; and Q represents the total diabatic heating rate associated with all sources of latent/sensible heating and radiative

forcing. Note that in the above system of anelastic equations, the subscripts (t, r, φ, z) denote partial derivatives in the corresponding directions, and $S \equiv g(\Gamma_d - \Gamma)/\overline{T}$ represents the atmospheric stratification in terms of the dry adiabatic lapse rate Γ_d and environmental lapse rate Γ.

Consider next a set of typical scales for TCs including the scales for the maximum radial wind in the boundary layer U, the maximum tangential wind near the surface V, the maximum vertical motion in the eyewall W, the absolute geopotential deficit between the vortex center and the eyewall $\Delta\Phi$, the radius of the maximum wind R, and the maximum buoyancy at the vortex center B. Note that in the pseudoheight coordinate, the thermodynamic equation is written in terms of the buoyancy variable b, and so the scale of the maximum buoyancy B will therefore correspond to a warm core at the TC center as $B \equiv gT'/\overline{T}(z)$, where T' denotes the maximum warm core at the vortex center with respect to far-field environment. Scale analysis of Eqs. (1)–(5) for the TC inner-core region under the axisymmetric approximation leads to

$$\frac{dU}{dt} \approx \mathcal{O}\left(-\frac{U^2}{R}\right) + \mathcal{O}\left(\frac{WU}{H}\right) + \frac{V^2}{R} - \frac{\Delta\Phi}{R} - \frac{C_D}{h} U|V|, \quad (6)$$

$$\frac{dV}{dt} \approx \mathcal{O}\left(\frac{UV}{R}\right) + \mathcal{O}\left(\frac{WV}{H}\right) - \frac{UV}{R} - \frac{C_D}{h} V|V|, \quad (7)$$

$$0 \approx -\frac{\Delta\Phi}{H} + B, \quad (8)$$

$$0 \approx \frac{U}{R} + \frac{W}{H}, \quad (9)$$

$$\frac{dB}{dt} \approx \frac{UB}{R} - SW + Q, \quad (10)$$

where the hydrostatic balance is used in Eq. (8) and the scale analysis for the fictional forces assumes the bulk formula for both the radial and tangential momentum equations in the PBL of depth h such that $F_{u,v} = \partial\tau_{u,v}/\partial z \approx \tau_{u,v}/h$. Here, $\tau_{u,v}$ are surface momentum fluxes parameterized as $\tau_u \approx C_D U\sqrt{U^2 + V^2} \approx C_D U|V|$ and similar for $\tau_v \approx C_D V|V|$, where C_D is the surface drag coefficient. Note that the scale analyses for the advective terms in the radial and tangential momentum equations have taken also into account the fact that $\partial u/\partial r \sim \partial v/\partial r \sim 0$ near the radius of maximum wind (RMW) and $w\partial u/\partial z \sim w\partial u/\partial z \sim 0$ because of weak vertical motion in the PBL. As such, the scales of these advective terms are of a higher order as compared to other terms near the RMW (Anthes 1974). In addition, the scale analysis for the partial derivative of w with height must consider that w is maximum in the layer between 500 and 300 hPa, and so $\partial w/\partial z \sim 2W/H$.

Because our main focus is in the inner-core region, the impact of the Coriolis force is hereinafter neglected in the all-scale estimation to simplify our analyses. Except for a more complex characteristic equation and eigenvalues, the inclusion of this Coriolis parameter can be shown to have minimal impacts on the MPI equilibrium (Kieu and Wang 2017). Upon substituting the relationships

$$W = -\frac{UH}{R} \quad \text{and} \quad \Delta\Phi = BH \quad (11)$$

that are obtained from Eqs. (8) and (9) into Eqs. (6), (7), and (10), and note that $U \ll V$, we have

$$\frac{dU}{dt} = \gamma V^2 - \frac{\gamma}{\alpha} B - \beta U|V|, \quad (12)$$

$$\frac{dV}{dt} = -\gamma UV - \beta V|V|, \quad (13)$$

$$\frac{dB}{dt} = \gamma UB + \sigma U + Q, \quad (14)$$

where $\gamma \equiv 1/R$, $\beta \equiv C_D/h$, $\alpha = 1/H$, and $\sigma \equiv SH/R$. Unlike the HSD system studied in K2015 that relies on the gradient wind balance, the above TC-scale system (12)–(14) uses the gradient wind unbalance so that evolution of the radial inflow u is explicitly taken into account in Eq. (12).

Following K2015, we will close the above system (12)–(14) by utilizing a bulk parameterization for the diabatic heating source Q, using the WISHE mechanism and the Newtonian cooling relaxation forcing so that the total diabatic heating Q is given by

$$Q \sim \eta \frac{gC_h}{h} \frac{(s_s - s_a)}{C_p \overline{T}} |V| + \kappa B, \quad (15)$$

where C_h is the coefficient for heat (sensible and latent) transfer, C_p is the constant pressure heat capacity, $s_{s,a}$ are the saturated enthalpy at the ocean surface and the actual enthalpy at the atmospheric layer right above the ocean surface, and $\kappa < 0$ represents the Newtonian radiative relaxation rate. Note in the above expression for the total heating, Q has been rearranged to have a correct dimension after taking into account the definition of buoyancy b in Eq. (10) [i.e., the factor $g/\overline{T}$ in Eq. (15) is required to convert from potential temperature to the buoyancy variable b]. Following Emanuel (1986), a factor η is also introduced in Eq. (15) to represent the efficiency of the energy conversion, which is determined by the difference between the sea surface temperature and the outflow temperature. This Carnot energy conversion factor will ensure that a critical point obtained from the TC-scale system will match Emanuel's MPI formula as will be seen in the next section.

Similar to the representations of the frictional force $F_{u,v}$, the total enthalpy associated with the temperature and moisture flux gradient within the PBL in the above expression for Q is approximated as τ_s/h, where the surface enthalpy flux τ_s is represented in terms of the saturated enthalpy at the ocean surface and the actual enthalpy at the atmospheric layer right above the ocean surface as $\tau_s \sim C_h(s_s - s_a)$. Physically, the closure in Eq. (15) implies that the total heating in the TC region is associated with the enthalpy flux at the ocean surface, part of which will be used to do work against the frictional force, and the remaining part will be exhausted at the outflow level.

Substituting Eq. (15) into Eq. (14), we obtain a system of equations describing the evolution of the TC scales as follows:

$$\frac{dU}{dt} = \gamma V^2 - \frac{\gamma}{\alpha} B - \beta U|V|, \tag{16}$$

$$\frac{dV}{dt} = -\gamma UV - \beta V|V|, \tag{17}$$

$$\frac{dB}{dt} = \gamma UB + \sigma U + \delta|V| + \kappa B, \tag{18}$$

where the parameter $\delta \equiv \eta(gC_h/h)[(s_s - s_a)/C_p\overline{T}]$. It should be mentioned that the absolute sign for $|V|$ in the WISHE parameterization in Eq. (15) and frictional force is important in Eqs. (16)–(18), because it determines the basin of the attraction between two domains $V > 0$ and $V < 0$, as will be shown in the next section. For the sake of discussion, the system (16)–(18) will be hereinafter referred to as a modified TC-scale dynamical (MSD) model to distinguish it from the HSD system presented in K2015.

Although the above scale analyses are mostly applicable for the mature stage, we propose that these scale analyses can be extended to other stages of the TC development as well so long as $U \ll V$. Indeed, previous observational and modeling studies have shown that the quasi-gradient balance can well describe the evolution of TC-like vortices for which gradient wind balance is maintained above the PBL during TC development (e.g., Hack and Schubert 1986; Willoughby 1990; Liu et al. 1999; Schubert et al. 2007). While gradient wind balance cannot be exactly applied in the PBL, the implication of this first-order gradient balance approximation is that radial inflow or vertical motion is always smaller than the tangential flow at different stages of the TC development, which suffices to derive the above TC-scale dynamic model in Eqs. (16)–(18). As such, we will postulate the validity of this modified TC-scale system for all stages of the TC development with a caution that the results obtained from this MSD model will be most suitable for the strong intensity stage. Such a caveat is not a severe limit of the MSD system, because our ultimate focus in this study is on the MPI equilibrium at the mature state. Therefore, this caveat of the TC-scale analysis will be alleviated as TCs approach their MPI equilibrium.

3. Stability analysis

a. Critical points

Before examining the critical points[1] of the MSD system and their associated stability, it is important to note two key properties of the MSD system that allow for much simplified stability analysis of the MSD system. First, it is readily seen from Eq. (17) that, similar to K2015's HSD system, the plane $V = 0$ acts as a separatrix in the phase space of (U, V, B), where the domain $V > 0$ is completely separated from the domain with $V < 0$. Exactly on the plane $V = 0$, flows will be strictly confined on this plane because $\dot{V} = 0$,[2] and so there is no possibility for an orbit starting in the domain $V > 0$ to cross the plane $V = 0$ and move to the other domain $V < 0$. This important property allows us to work exclusively in the domain $V > 0$ or $V < 0$ without the need to consider possibilities of a flow crossing each other in the absence of Coriolis force. Because of the symmetry of the MSD system under the change of the variable $V \to -V$, the MSD system is valid in both hemispheres similar to the HSD system examined in K2015. Given the dominant cyclonic flow in the Northern Hemisphere, we will herein focus on the regime $V > 0$ such that all absolute value signs in the MSD system (16)–(18) can be neglected. All analyses for the Southern Hemisphere can be readily reproduced by simply replacing V by $-V$ in the MSD system. Detailed treatment of the Coriolis force is given in appendix A.

A second important observation is that the divergence of the forcing $\mathbf{f}$ of the MSD system [i.e., the right-hand sides (RHSs) of Eqs. (16)–(18)] is not constant but depends on the flow regime. Indeed, a direct calculation of $\nabla \cdot \mathbf{f}$, where $\mathbf{f}$ denotes the forcing vector on the right-hand side of the MSD system, shows that $\nabla \cdot \mathbf{f} = -3\beta V + \kappa$. Given that $\kappa < 0$ and $V > 0$, it is apparent that the MSD system is dissipative. This means that any initial small volume in the phase space will shrink continuously, thus exhibiting all typical behaviors

[1] By definition, critical points $\mathbf{x}_c$ of a dynamical system $\dot{\mathbf{x}} = \mathbf{F}(\mathbf{x})$ refer to the points in the phase space at which the forcing $\mathbf{F}(\mathbf{x}_c) = 0$.

[2] It can be proven that there exist in fact periodic orbits on the plane $V = 0$ that involve only U and B.

of a dissipative system as long as we confine within the regime $V > 0$.

To facilitate comparison with K2015's model, we consider first the simplest case of neutral stratification without radiative cooling such that $\sigma = \kappa = 0$ and restrict our analysis to the regime $V > 0$. In this case, Eqs. (16)–(18) are reduced to

$$\frac{dU}{dt} = \gamma V^2 - \frac{\gamma}{\alpha} B - \beta UV, \tag{19}$$

$$\frac{dV}{dt} = -\gamma UV - \beta V^2, \tag{20}$$

$$\frac{dB}{dt} = \gamma UB + \delta V, \quad \forall V \in \Omega. \tag{21}$$

It is noticed that the system (19)–(21) possesses one zero critical point (0, 0, 0) and the two other nonzero critical points (U_c, V_c, B_c), which are the roots of the RHSs of Eqs. (19)–(21) and given as follows:

$$U_c = -\frac{\beta V}{\gamma}, \quad V_c = \pm\sqrt{\frac{\delta}{\alpha\beta}\frac{\gamma^2}{\gamma^2+\beta^2}}, \quad B_c = \frac{\delta}{\beta}. \tag{22}$$

Because we limit our analysis to flow in the domain Ω with $V > 0$, the critical point corresponding to the minus sign of V_c will not be herein considered. A quick examination of the critical point U_c, V_c, B_c in Eq. (22) shows that the value of B_c in Eq. (22) is identical to the value of B_c in the HSD system studied in K2015, while V_c in Eq. (22) is very close to the value of V_c obtained in the HSD system despite very different underlying balance approximations for the vertical and the radial momentum equations.

For an explicit comparison, recall that the HSD model presented in K2015 is based on the gradient wind balance and the nonhydrostatic balance and results in a critical point V_c given by

$$V_c^2 = \frac{\delta}{\alpha\beta}, \tag{23}$$

which can be shown to be identical to Emanuel's MPI formula $V_{\mathrm{MPI}}^2 = (C_h)/(C_d)[(T_s - T_0)/\overline{T}_s](s_s - s_a)$ upon substituting all of the parameters α, β, and δ into Eq. (23) (see K2015). Comparison of the value of V_c obtained from the MSD system [i.e., Eq. (22)] and that obtained from the HSD system [i.e., Eq. (23)] shows that the two differ only by a factor $\gamma/(\gamma^2+\beta^2)^{1/2}$. An estimation of this factor using typical values of $R \sim 30$ km, $C_D = 10^{-3}$, and $h \sim 1$ km shows that $\beta = C_D/h \ll \gamma$, and so $\gamma^2/(\gamma^2+\beta^2) \sim 1$. Hence, the values of V_c at the MPI critical point in both the MSD and HSD models are very similar in spite of different balance approximations. In fact, direct inspection of the critical points U_c and V_c given by Eq. (22) shows that $U_c^2 + V_c^2 = \delta/(\alpha\beta)$, which is identical with the value V_c obtained from the HSD model [cf. Eq. (23)]. This is physically expected, because the gradient wind imbalance in the MSD system introduces an additional component of the radial inflow, and the projection of the horizontal wind vector on the tangential direction is therefore reduced. As a result, the MPI value V_c obtained from the MSD system is slightly weaker than the MPI value obtained from the HSD system in K2015.

That the values of the MPI critical point V_c obtained from two different models are similar regardless of the use of the hydrostatic or the gradient balance approximation is interesting. At the deepest essence, this result indicates the unique nature of the MPI equilibrium that does not appear to depend on the gradient wind imbalance or the nonhydrostatic correction. This may help explain why various models for TC development based either on the gradient wind balance or the hydrostatic approximation capture an MPI equilibrium similar to full-physics models at the TC mature stage. Of course, this similarity does not imply that the gradient wind imbalance is unimportant in TC development, as it is ultimately the imbalance in the PBL that drives the evolution of a TC vortex. However, in the asymptotic limit of $t \to \infty$, it does suggest that the restricted form of the gradient wind imbalance as given by Eq. (12) has little effect on the stability property of the MPI equilibrium or the value of the MPI limit.

Of further significance is that the critical point in Eq. (22) exhibits an explicit relation between the scales of the maximum radial inflow and the tangential wind (i.e., $U_c = \beta V_c/\gamma$). Such a relationship between these two scales is consistent with the well-documented observation of $U \ll V$ used in numerous theoretical models of the TC structure (e.g., Willoughby 1979). Indeed, use of the typical scale for $R \sim 30$ km, $h = 1$ km, and $C_D = 10^{-3}$ confirms that U_c is one order of magnitude smaller than V_c, a fact well obtained from both observational and modeling studies but has not been well understood from the dynamical perspective. Although the value of $U_c \sim 5$ m s^{-1} appears to be smaller than a typical value of the maximum radial inflow for a storm with $V_c = 65$ m s^{-1} because of the neglect of detailed eyewall processes, that U_c is indeed much smaller than V_c as obtained from Eq. (22) is critical, because it indicates the MSD system provides a self-consistent relationship among the TC scales as assumed in deriving Eq. (12).

The relation between U_c and V_c as given by Eq. (22) reveals also how the scale of the radial inflow depends on other parameters such as the depth of the PBL h and the drag coefficient C_D. For example, a direct implication of Eq. (22) is that a thinner PBL or a larger

drag coefficient C_D would correspond to stronger inflow given the same value of the maximum tangential wind. In this regard, the MSD system not only provides an expected MPI limit but also justifies the relationships among different scales of TCs, which have not been rigorously addressed in previous studies.

Given the critical point (U_c, V_c, B_c) in Eq. (22), we next follow a similar approach to K2015 and use these values to nondimensionalize the general MSD system (19)–(21) for our subsequent stability analysis. Defining $U = |U_c|u^*$, $V = V_c v^*$, $B = B_c b^*$, and $t = Tt^*$, where the superscript asterisk denotes nondimensionalized variables, we obtain

$$\frac{du^*}{dt^*} = \frac{\gamma T V_c^2}{|U_c|} v^{*2} - \frac{\gamma T B_c}{\alpha |U_c|} b^* - \beta T V_c u^* v^*, \quad (24)$$

$$\frac{dv^*}{dt^*} = -\gamma T |U_c| u^* v^* - \beta T V_c v^{*2}, \quad (25)$$

$$\frac{db^*}{dt^*} = \gamma T |U_c| b^* u^* + \frac{\sigma T |U_c|}{B_c} u^* + \frac{\delta T V_c}{B_c} v^* + \kappa T b^*. \quad (26)$$

Using the scale constraints at the critical point given by Eq. (22) and neglecting the asterisk hereinafter with an implicit convention that lowercase letters represent nondimensional variables to simplify our notation, we arrive at a set of nondimensionalized equations for the scale dynamics of TCs as follows:

$$\frac{du}{dt} = \frac{\gamma^2 T V_c}{\beta} v^2 - \frac{T V_c (\gamma^2 + \beta^2)}{\beta} b - \beta T V_c uv, \quad (27)$$

$$\frac{dv}{dt} = -\beta T V_c (uv + v^2), \quad (28)$$

$$\frac{db}{dt} = \beta T V_c bu + \frac{\sigma \beta^2 T V_c}{\gamma \delta} u + \beta T V_c v + \kappa T b. \quad (29)$$

This system can be further simplified if we choose a time scale T such that $T\beta V_c = 1$. Substitute $T = 1/(\beta V_c)$ in the system (27)–(29), and we have

$$\frac{du}{dt} = pv^2 - (p+1)b - uv, \quad (30)$$

$$\frac{dv}{dt} = -uv - v^2, \quad (31)$$

$$\frac{db}{dt} = bu + su + v - rb, \quad (32)$$

where $p \equiv (\gamma/\beta)^2$, $s \equiv (\sigma\beta)/(\gamma\delta)$, and $r = -\kappa T > 0$. For the sake of convenience, Table 1 lists typical values of all parameters in the MSD system (30)–(32). With the nondimensional form, the critical point (U_c, V_c, B_c) of the MSD system (30)–(32) is now simply (−1, 1, 1) in the absence of stratification and radiative cooling (i.e., $r = s = 0$), and it will be referred to hereinafter as the MPI critical point, because its v component displays a similar value as the MPI limit.

In the presence of both radiative cooling and stratification, the critical point of Eqs. (30)–(32) is no longer (−1, 1, 1) but is shifted to a slightly different point in the phase space of (u, v, b). Indeed, the only positive critical point of the system (30)–(32) in the presence of radiative forcing and tropospheric stratification is now given by

$$u_c = -v_c, \quad v_c = \frac{-r + \sqrt{r^2 + 4(1-s)}}{2}, \quad b_c = \frac{(1-s)v_c}{v_c + r}, \quad (33)$$

where only the root of a quadratic equation for v_c with a plus sign is selected in Eq. (33) because of our restriction on the domain $v > 0$.

A number of interesting results can be derived from the expression for the MPI critical point given by Eq. (33). First, we recall that the parameters r and s represent the effects of the radiative cooling and stratification of the troposphere on the TC development, whose range is typically $\in [0, 1]$ in the nondimensional unit. Direct inspection of v_c given by Eq. (33) shows that v_c depends more sensitively on the stratification parameter s than on the radiative forcing parameter r. Specifically, as the radiative forcing becomes stronger, the MPI limit decreases roughly as a linear function because of the reduction of the warm-core amplitude at the MPI equilibrium (see Fig. 1a), which is consistent with the modeling study by Rotunno and Emanuel (1987).

The dependence of v_c on s is somewhat more subtle, as v_c decreases rapidly when s increases (Fig. 1b). Indeed, for $r \ll 1$, v_c can be approximated as $v_c \approx \sqrt{1-s}$, which is given in the full dimensional form as follows:

$$V_c^2 \approx V_{\mathrm{MPI}}^2 \left[1 - \frac{gH^2(\Gamma_d - \Gamma)}{V_{\mathrm{MPI}}^2 \overline{T}}\right], \quad \text{where}$$

$$V_{\mathrm{MPI}}^2 = \frac{C_h}{C_d} \frac{(T_s - T_0)}{\overline{T}_s} (s_s - s_a). \quad (34)$$

Expression (34) for the MPI critical point V_c is noteworthy, as it reveals an explicit dependence of the MPI limit on the tropospheric stratification measured in terms of $(\Gamma_d - \Gamma)$; the more stable the tropospheric stratification is [i.e., the larger $(\Gamma_d - \Gamma)$], the weaker the MPI limit would be. This result is physically reasonable, because a stable troposphere tends to be inimical to the development of deep convection and thus limits the

TABLE 1. Table of values of tropical cyclone scales and related parameters.

Parameter	Value	Remark	Reference
V_c	$\sim 65\ \mathrm{m\ s^{-1}}$	Typical scale of the maximum tangential wind at the critical point for SST of 30°C	Assigned
U_c	$\sim 5\ \mathrm{m\ s^{-1}}$	Scale of the radial wind at the critical point ($U_c = RC_DV_c/h$)	Derived from Eq. (22)
B_c	$\sim 0.4\ \mathrm{m\ s^{-2}}$	Scale of the maximum buoyancy that corresponds to the warm core at the vortex center [$B_c = V_C^2\alpha(\gamma^2+\beta^2)/\gamma^2$]	Derived from Eq. (22)
S	$\sim 5\times10^{-4}\ \mathrm{s^{-2}}$	Tropospheric stratification [$S \equiv g(\Gamma_d - \Gamma)/\overline{T}$]	Assigned
$\Delta\Phi$	$\sim 4000\ \mathrm{m^2\ s^{-2}}$	Scale of the geopotential deficit between the vortex center and the radius of maximum wind ($\Delta\Phi = B_cH$)	Derived from Eq. (8)
H	$\sim 10^4$ m	Scale height of the troposphere	Assigned
h	$\sim 10^3$ m	Depth of the PBL	Assigned
C_D	$\sim 1.5\times10^{-3}$	Surface drag coefficient	Assigned
R	$\sim 50\times10^3$ m	Radius of the maximum tangential wind	Assigned
γ	$\sim 2\times10^{-5}\ \mathrm{m^{-1}}$	Inverse of the radius of the maximum wind ($\gamma = 1/R$)	Definition
α	$\sim 10^{-4}\ \mathrm{m^{-1}}$	Inverse of the scale height H ($\alpha = 1/H$)	Definition
β	$\sim 1.5\times10^{-6}\ \mathrm{m^{-1}}$	Ratio of the surface drag to the PBL depth ($\beta = C_D/h$)	Definition
δ	$\sim 5\times10^{-5}\ \mathrm{s^{-2}}$	WISHE feedback parameter ($\delta = \beta B_c$)	Derived from Eq. (22)
κ	$\sim 10^{-5}\ \mathrm{s^{-1}}$	Newtonian cooling relaxation rate	Assigned
T	$\sim 10^4$ s	Characteristic time scale [$T \equiv 1/(\beta V_c) = h/C_DV_c$]	Definition
p	~ 178	Nondimensional square ratio of the PBL depth over the RMW [$p \equiv (\gamma/\beta)^2 = (h/RC_D)^2$]	Definition
r	~ 0.1	Nondimensional parameter representing the radiative cooling ($r \equiv \kappa T = \kappa h/C_DV_c$)	Definition
s	~ 0.15	Nondimensional parameter representing the tropospheric stratification ($s \equiv S\beta/\alpha\delta$)	Definition

maximum potential intensity that a storm can attain. Such impact of the tropospheric stratification as derived from Eq. (34) is in good agreement with a number of previous modeling studies (Shen et al. 2000; Tuleya et al. 2016; Hill and Lackmann 2011). In fact, Hill and Lackmann (2011) suggested that the tropospheric stabilization could offset as much as 50% of the increase in TC intensity related to warmer SST in their experiments.

While the above expression for the MPI limit explicitly contains the stratification factor, it is important to note that the atmospheric stratification is not a free parameter, but it is generally a function of multiple atmospheric conditions such as SST, tropopause temperature, or moisture structure that is constrained by the radiative–convective equilibrium. Because of this interrelation among the large-scale parameters, the variability of the MPI limit should be a multivariate function of atmospheric conditions beyond the direct SST dependence as dictated by Emanuel's MPI formula. The specific dependence of the MPI limit on the atmospheric stratification as given by Eq. (34) is significant, because it reveals subtle impacts of the tropospheric stratification on TC intensity variability, which to our knowledge has not been demonstrated previously. In this regard, Eq. (34) can be used to validate the applicability of the MSD system in a full-physics model framework, which we will present in our upcoming study.

Second, in the presence of the strong tropospheric stratification and radiative cooling, one notices an intricate behavior of critical point v_c given by Eq. (33) similar to that in the HSD system (see appendix 1 in K2015). Specifically, the critical point v_c will be pulled toward the origin (0, 0, 0) as the parameter $s \to 1$, and it merges with the zero critical point (0, 0, 0) for $s = 1$, resulting in a saddle-node bifurcation. For an even more stable troposphere such that $s > (r^2+4)/4$, the MPI critical point completely disappears, and the TC development would never occur. As a result, one would expect the tropospheric stratification to be close to neutral so that an incipient vortex could grow. Such a critical role of the tropospheric stratification obtained from the MSD system to some extent supports the previous finding about the decrease of the MPI limit due to changes of the stratification in the outflow layer discussed in Emanuel and Rotunno (2011). Of course, this consistency with Emanuel and Rotunno (2011)'s study is by no means exact, because Emanuel and Rotunno (2011)'s study is mostly concerned with the stratification of the outflow layer, whereas our MSD system focuses on the stratification of the entire tropospheric depth.

From the dynamical perspective, the existence of critical points alone is not sufficient to depict the full evolution or stability of a dynamical system. Any analyses of the critical-point stability would require specific

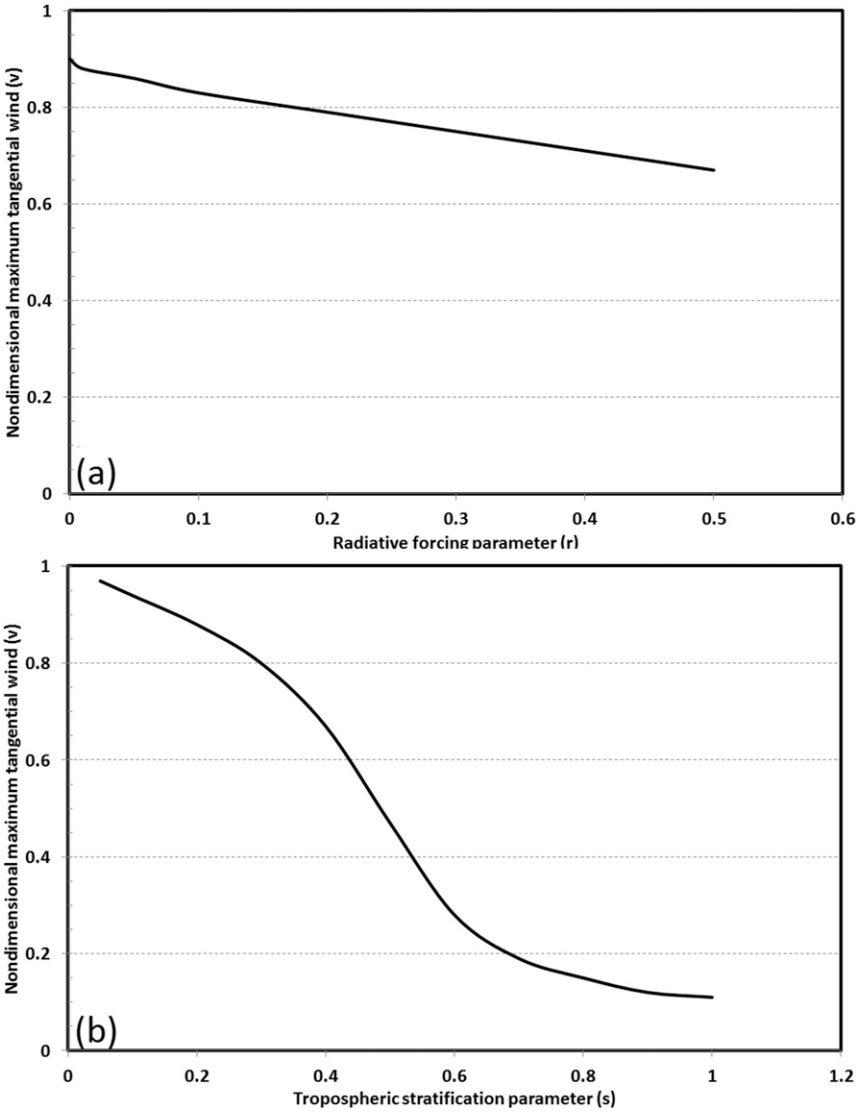

FIG. 1. (a) Dependence of the maximum tangential wind v at the MPI equilibrium on the radiative forcing parameter r in the MSD system (30)–(32), and (b) as in (a), but for the dependence of v on the tropospheric stratification parameter s in the MSD system.

properties of the linearized Jacobian matrix at the critical points, to which we now turn.

b. *Linear stability analysis*

In this section, we will examine the stability of the MPI critical point $\mathbf{x}_c \equiv (u_c, v_c, b_c)$ given by Eq. (33) for the general MSD system in the presence of both the stratification and the radiative cooling (i.e., $r \neq 0$ and $s \neq 0$). Our aim is to show that this critical point is asymptotically stable, and its stability is furthermore continuous in the parameter space (p, r, s). As a consequence, (u_c, v_c, b_c) is locally structurally stable, thus establishing the stable property for the MPI equilibrium as seen from previous modeling studies.

We first linearize the MSD system around the critical point (u_c, v_c, b_c) by setting $u = u_c + x$, $v = v_c + y$, and $b = b_c + z$, where (x, y, z) are small perturbations, to obtain

$$\frac{dx}{dt} = -v_c x + (2pv_c - u_c)y - (p+1)z, \tag{35}$$

$$\frac{dy}{dt} = -v_c x - 2v_c y, \tag{36}$$

$$\frac{dz}{dt} = (b_c + s)x + y - rz. \tag{37}$$

The Jacobian matrix for the MSD system (30)–(32) at $\mathbf{x}_c$ is therefore given by

$$\left.\frac{\partial \mathbf{F}(\mathbf{x})}{\partial \mathbf{y}}\right|_{\mathbf{x}_c} = \begin{pmatrix} -v_c & 2pv_c - u_c & -p-1 \\ -v_c & -u_c - 2v_c & 0 \\ b_c + s & 1 & u_c - r. \end{pmatrix}. \quad (38)$$

Direct calculation of eigenvalues for the Jacobian matrix leads to the following characteristic equation:

$$\lambda^3 + A\lambda^2 + B\lambda + C = 0, \quad (39)$$

where

$$A(\mathbf{x}_c, p, r, s) = 3v_c + r, \quad (40)$$

$$B(\mathbf{x}_c, p, r, s) = 2(p+1)v_c^2 + 2v_c(v_c + r) + (p+1)\frac{v_c + rs}{r + v_c}, \quad (41)$$

$$C(\mathbf{x}_c, p, r, s) = (p+1)(b_c v_c + s v_c) + (v_c + r)2(p+1)v_c^2 - (p+1)v_c, \quad (42)$$

Note here the continuous dependence of the coefficients A, B, and C on the model parameters (p, r, s), which facilitates our later examination of the local structural stability. Recall that the critical point $\mathbf{x}_c$ is stable if and only if the cubic Eq. (39) possesses all three roots with negative real parts. The existence of three roots with negative real parts is guaranteed if the following conditions for the coefficients A, B, and C are applied (see, e.g., Abramowitz and Stegun 1972, 17–18; Ma and Wang 2011):

$$A(\mathbf{x}_c, p, r, s) > 0, \quad C(\mathbf{x}_c, p, r, s) > 0, \quad (43)$$

$$A(\mathbf{x}_c, p, r, s)B(\mathbf{x}_c, p, r, s) - C(\mathbf{x}_c, p, r, s) > 0, \quad (44)$$

With the exact expression for the critical point as given by (33), the explicit expressions for A, B, and C are given by

$$A(\mathbf{x}_c, p, r, s) = 3\sqrt{\frac{r^2}{4} + 1 - s} - \frac{r}{2} > 0, \quad (45)$$

$$B(\mathbf{x}_c, p, r, s) = (p+1)\left(\frac{3v_c^2 - 2sv_c^2 + rsv_c}{1-s} + \frac{2-2s}{p+1}\right) > 0, \quad (46)$$

$$C(\mathbf{x}_c, p, r, s) = (p+1)(v_c^3 + v_c - sv_c) > 0, \quad (47)$$

and the condition (44) therefore becomes

$$A(\mathbf{x}_c, p, r, s)B(\mathbf{x}_c, p, r, s) - C(\mathbf{x}_c, p, r, s) = (p+1)\left[\left(3\sqrt{\frac{r^2}{4} + 1 - s} - \frac{r}{2}\right)\left(\frac{3v_c^2 - 2sv_c^2 + rsv_c}{1-s} + \frac{2-2s}{p+1}\right) - (v_c^3 + v_c - sv_c)\right]. \quad (48)$$

Use the following identity

$$3\sqrt{\frac{r^2}{4} + 1 - s} - \frac{r}{2} = 3\sqrt{\frac{r^2}{4} + 1 - s} - \frac{3r}{2} + r = 3v_c + r,$$

and note that for $0 < r, s < 1$,

$$\frac{3v_c^2 - 2sv_c^2 + rsv_c}{1-s} + \frac{2-2s}{p+1} > \frac{3v_c^2 - 2sv_c^2 + rsv_c}{1-s} > 2v_c^2,$$

we obtain

$$A(\mathbf{x}_c, p, r, s)B(\mathbf{x}_c, p, r, s) - C(\mathbf{x}_c, p, r, s) > (p+1)[(3v_c + r)2v_c^2 - v_c^3 - v_c + sv_c] = (p+1)v_c(5v_c^2 + 2rv_c + s - 1) = (p+1)v_c(4v_c^2 + rv_c) > 0. \quad (49)$$

Apparently, both conditions (43) and (44) are satisfied at the critical point $\mathbf{x}_c$, and the characteristic Eq. (39) thus possesses all roots with negative real parts (see appendix B for explicit expressions for the eigenvalues of the Jacobian matrix evaluated at the critical point $\mathbf{x}_c$). As a result, the MPI critical point $\mathbf{x}_c$ is asymptotically stable as expected. Because all eigenvalues of the Jacobian matrix (38) are continuously dependent on (p, r, s) and the nonzero critical point in Eq. (33) is hyperbolic, $\mathbf{x}_c$ is not only asymptotically stable but also locally structural stable, based on the Hartman–Grobman theorem (Alligood et al. 1996). For the zero critical point (0, 0, 0), it is easy to see that this critical point is an unstable node, and the MSD system has indeed only one stable point $\mathbf{x}_c$ in the domain $v > 0$ given by Eq. (33).

That the MPI equilibrium is unique and structurally stable in the domain $v > 0$ has an important consequence

in study of TC development. As discussed in the introduction section, this stability indicates that regardless of the vortex initial condition with which one initializes a TC model, the final stage of TC intensity will be unique, and it is determined by the large-scale environment as given by the MPI limit (e.g., Emanuel 2000). As long as the favorable environmental conditions are maintained, the incipient vortex will soon approach its MPI equilibrium, a result very similar to that obtained in the HSD system (K2015).

On the other hand, the existence of a unique stable point in the MSD system indicates that the ω-forward limit set of the MSD system consists of a single point, and so all intensity variation would have to asymptotically approach zero. As discussed in Kieu and Moon (2016), this asymptotically zero intensity growth turns out to be inconsistent with the saturation of TC intensity errors around 8–10 m s^{-1} as obtained from the real-time verification of TC intensity forecasts. This inconsistency between the MSD ω-forward set and the intensity error saturation reflects the shortcoming of the MSD system in representing the full dynamics of TCs whose MPI attractor has much more complex structure (Kieu and Moon 2016). Therefore, the full characteristics of the MPI attractor have to be resolved with full-physics model simulations, which are, however, beyond the scope of the MSD system in this study.

As a demonstration of the stability of the MPI equilibrium, Fig. 2 shows several examples of flow orbits in the phase space of (u, v, b) for a range of initial conditions, using the Runge–Kutta fourth-order scheme with a time step $\Delta t = 0.001$ ($\sim$10 s in the full dimensional unit). Despite much different initial conditions, these orbits all converge to the same critical point as expected, thus confirming the above linear stability analyses. Note that the aforementioned stability analysis by no means ensures the global stability or dictates the basin of attraction around the critical point. An important question regarding the basin of the attraction of the MPI point is much harder to quantify and has to be addressed from a numerical perspective. Our various sensitivity experiments with the MSD system show that the domain of attraction for the MPI critical point appears to be sufficiently large and includes all points in the domain $D \equiv (u, v, b | u \le 0, v > 0, b \ge 0)$. From a practical standpoint, this large basin of attraction implies that all initial data points are almost guaranteed to grow if $v > 0$, a fact that has been indeed well documented in modeling studies of TC development.

c. *The frequency of oscillation near stable critical points*

The numerical solutions illustrated in Figs. 2 and 3 reveal an interesting property that every trajectory $x(t)$

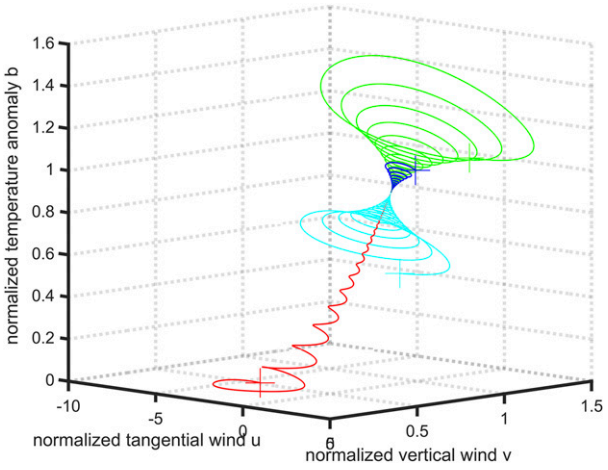

FIG. 2. Flow trajectories in phase space (u, v, b) for four different initial points in the phase space of (u, v, b) that represent an incipient weak vortex (0, 0.1, 0.1) (red); a mature TC near the MPI equilibrium with a too-weak warm core (−1, 1, 0.5) (cyan); a mature TC with intensity significant above the MPI equilibrium limit (−1, 1.4, 1) (green); and a mature TC near the MPI equilibrium limit with too-weak low-level convergence (−0.1, 1, 1) (blue).

appears to possess two different time scales: one is a short time scale associated with a rapid oscillation of period $\sim$0.2 unit time ($\approx$1 h) and the other much longer time scale at $\sim$5 unit times ($\approx$18 h) as the flows approach the critical point. The existence of the two different time scales is to some extent similar to the well-known two time scales in Lorenz's three-variable model; the slower time scale represents the duration of an orbit residing in one sector of the Lorenz attractor, and the other faster time scale represents the oscillation around the unstable point inside each sector (Palmer 1993).

For our MSD system, the two different time scales are seen for all orbits in the phase space (U, V, B) and signify that the development of TCs is not a simple linear growth as often assumed in previous studies (e.g., Charney and Eliassen 1964; Yanai 1964; Ooyama 1969). Instead, the tangential wind experiences a rapid spinup for a few hours and is then followed by a break before it resumes its amplification, as seen in Fig. 3a. In fact, the same phenomenon is also seen in the HSD model even under the exact gradient wind balance and nonhydrostatic approximation (K2015). The consistent behaviors of these two distinct time scales between the MSD and HSD models suggest that the TC development inherently possesses more subtle characteristics than the traditional linear growth.

To quantify the frequency of the short time scale in the MSD system, we observe one important property from our numerical experiments with the MSD system that the frequency associated with this short time scale

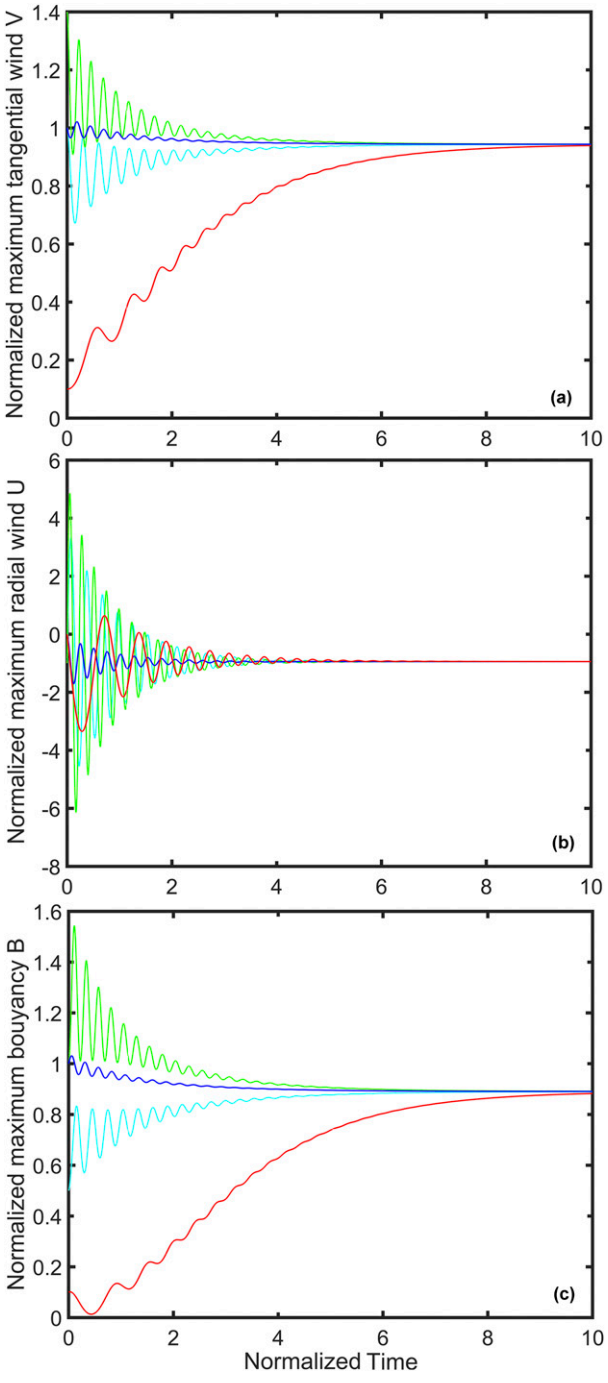

FIG. 3. Time evolution of (a) the nondimensionalized maximum tangential wind v, (b) the maximum radial wind u, and (c) the maximum buoyancy variable b for four different initial points illustrated in Fig. 2. Note that one unit of time corresponds to ~3 h, and the MPI equilibrium is located roughly at (−0.86, 0.86, 0.86) in the limit of small radiative forcing ($r = 0.1$) and weak tropospheric stratification ($s = 0.1$).

is maintained during the entire period as a flow approaches its MPI critical point (see Fig. 3). At the asymptotic limit of $t \to \infty$, this fast frequency $\omega(t)$ will approach a limit ω_0, which is the frequency evaluated at the MPI critical point. This observation suggests that the fast frequency $\omega(t)$ can be estimated as $\omega_0 \equiv \Im[\lambda(\mathbf{x}_c)]$ at $t \to \infty$, where $\Im[\lambda(\mathbf{x}_c)]$ is the imaginary part of the complex eigenvalue of Eq. (38) at the MPI critical point $\mathbf{x}_c$.

Given this observation, we can therefore obtain an estimation for the fast frequency ω_0 as a function of the model parameters (p, r, s) by working specifically at the MPI point. The general expression for ω_0 as a function of the full parameter (p, r, s) is complicated. However, an explicit expression for this fast frequency can be approximated for a simple case in which the radiative forcing is sufficiently small as follows:

$$\omega_0(p,0,s) = \frac{\sqrt{3}}{2}\left[\frac{-R}{2} + \left(\frac{R^2}{4} + \frac{Q^3}{27}\right)^{1/2}\right]^{1/3} + \frac{\sqrt{3}}{2}\left[\frac{-R}{2} - \left(\frac{R^2}{4} + \frac{Q^3}{27}\right)^{1/2}\right]^{1/3}, \tag{50}$$

where the functions R and Q are defined as

$$Q = \frac{3a_2 - a_1^2}{3} \quad \text{and} \quad R = \frac{2a_1^2 - 9a_1a_2 + 27a_3}{27}, \tag{51}$$

and the coefficients a_1, a_2, and a_3 are, respectively, given by

$$a_1 = 3\sqrt{1-s}, \quad a_2 = (p+1)(3-2s) + 2 - 2s, \quad a_3 = 2\sqrt{1-s}(1-s). \tag{52}$$

If we assume further that the atmosphere is close to neutrality such that $s \ll 1$, the above expression for the fast frequency is reduced to

$$\omega_0(p,0,0) = \frac{\sqrt{3}}{2}\left[\frac{3}{2}p + \frac{7}{6} + \left(p^3 + \frac{17}{4p^2} + \frac{29}{6}p + \frac{179}{108}\right)^{1/2}\right]^{1/3} + \frac{\sqrt{3}}{2}\left[\frac{3}{2}p + \frac{7}{6} - \left(p^3 + \frac{17}{4p^2} + \frac{29}{6}p + \frac{179}{108}\right)^{1/2}\right]^{1/3}. \tag{53}$$

For a sufficiently large value of the parameter p (see Table 1), this internal fast oscillation frequency turns out to be mostly proportional to $\sqrt{p}$, as speculated in K2015. Using the definition of the parameter p (see Table 1), it is seen that this fast frequency in the full dimensional form is

ultimately expressed as $\omega \sim V_c/R$; that is, the smaller the radius of the maximum wind R, the faster the storm intensity will fluctuate given the same MPI limit. Our various sensitivity experiments with the full MSD system (30)–(32) show that this estimation of the fast frequency is reasonably good even in the presence of both the radiative forcing and the tropospheric stratification, provided that $s < 0.1$ (not shown).

Physically, such a fast oscillation reflects the nature of the TC-scale model given by Eqs. (30)–(32). Assume that v increases too fast at some instance of time, then the WISHE feedback would lead to a stronger increase of the buoyancy (i.e., warm core), thus enhancing the radial inflow u in the PBL as given by Eq. (30). Such an increase of the inflow would in turn lead to stronger advection of the AAM and help spin up the tangential wind v so rapidly that the centrifugal force would soon dominate the right-hand side of Eq. (30). As a result of this rapid increase of the centrifugal force, the radial wind is reduced, leading to a break on the AAM advection and subsequently a slowdown of the tangential wind spinup. As seen from Eq. (30), the time scale of this process is proportional to $\sqrt{p}$, and explains the fast frequency as seen in Fig. 3. Because of the connection between the radial and vertical motions as constrained by the continuity equation, it turns out that a similar mechanism related to the rapid oscillation of w can justify the fast frequency in the HSD system as presented in the next section.

In contrast to the fast oscillation associated with the competition between the centrifugal force and the inward pressure gradient, the other slower frequency is determined by the balance between the advection of the AAM and the frictional force in the tangential momentum in Eq. (31). This slow frequency can be deduced if one notes that the frictional force $\sim v^2$ in Eq. (31) becomes significant only when the tangential flow is sufficiently large. Thus, the spinup of the tangential flow v can be slowed down only when the frictional force is comparable to the AAM advection. Indeed, a direct inspection of Eq. (31) shows that this long time scale is $\sim 1/|u_c| \approx 1$,[3] which is much longer than the short time scale associated with the fast oscillation $\sim 1/\sqrt{p} \approx 0.1$ mentioned above. These different underlying mechanisms account for two different time scales during the TC development as seen in Fig. 3a.

It is of interest to note that the nature of the fast oscillation during the TC development due to the imbalance between the centrifugal force and the inward pressure gradient in the radial momentum equation as described above is very similar to the oscillation of a ring mode in the TC inner-core region (Kieu 2016). Using the gradient wind balance to define a mean state for the inner core of a TC-like vortex, Kieu (2016) showed that an internal oscillation frequency around a balanced vortex with the maximum tangential wind V and the radius of maximum wind R is proportional to V/R. Similar to the fast frequency in the MSD system, the restoring force in both the MSD model and the balanced wave model is the imbalance between the centrifugal force and the pressure gradient. Of course, this similarity is somewhat superficial, as the wave model presented in Kieu (2016) is frictionless and applied strictly for the stationary background vortex, whereas the fast oscillation presented in this study is for an evolving storm. However, the same nature of the restoring force for the fast oscillation between these two studies indicates that the gradient wind imbalance appears to be the primary factor responsible for the fast fluctuation of the TC intensity during TC development.

4. Discussion

The fact that the extended TC-scale model presented in this study could provide consistent results with the HSD model in K2015, despite different underlying approximations, is very intriguing. Specifically, the HSD model employs the gradient wind balance and the nonhydrostatic approximation, whereas the MSD model is based on gradient wind imbalance and hydrostatic balance. In both models, we obtain a very similar value of the MPI critical point [apart from a small factor $\sim\sqrt{\gamma^2/(\gamma^2+\beta^2)}$] for the maximum tangential wind, the same asymptotic stability for the MPI point, and the same characteristic of the fast and slow time scales during TC development.

This consistency between the HSD and the MSD models turns out to be understandable if one recalls the particular diagnostic role of the continuity equation. Under the Boussinesq approximation, the continuity equation will simultaneously determine either U or W if we know the other. As such, the inclusion of both the radial momentum equation and the nonhydrostatic approximation does not lead to a new

[3] A rough estimation of the longer time scale can be seen by directly integrating Eq. (31), assuming the largest inflow value u_c, which gives $v(t) = (|u_c|e^{|u_c|t})/(1 + |u_c|e^{|u_c|t})$. Thus, the longer time scale is proportional to $2.7/|u_c|$, or roughly $2.7h/(C_h V_c)$ in the full dimensional form.

prognostic equation in the framework of scale analysis. To understand further the implication of this diagnostic nature of the continuity equation, assume one extends the MSD system (30)–(32) by including the vertical momentum equation in the nonhydrostatic form as follows (see K2015):

$$\frac{dU}{dt} = \gamma V^2 - \gamma\Delta\Phi - \beta UV, \tag{54}$$

$$\frac{dV}{dt} = -\gamma UV - \beta V^2, \tag{55}$$

$$\frac{dW}{dt} = -\alpha\Delta\Phi + B, \tag{56}$$

$$\frac{dB}{dt} = \gamma UB + \sigma U + Q. \tag{57}$$

Substitute the relationship $U = -WR/H \equiv -\alpha W/\gamma$ that is obtained from the continuity equation into Eq. (54), and we have

$$\frac{dW}{dt} = -\frac{\gamma^2}{\alpha}V^2 + \frac{\gamma^2}{\alpha}\Delta\Phi + \frac{\beta\gamma}{\alpha}UV. \tag{58}$$

The consistency between the radial momentum equation [Eq. (58)] and the vertical momentum equation [Eq. (56)] under the Boussinesq constraint is therefore ensured if and only if

$$-\frac{\gamma^2}{\alpha}V^2 + \frac{\gamma^2}{\alpha}\Delta\Phi + \frac{\beta\gamma}{\alpha}UV = -\alpha\Delta\Phi + B, \tag{59}$$

from which

$$\Delta\Phi = \frac{1}{\alpha^2+\gamma^2}(\gamma^2V^2 + B\alpha - \beta\gamma UV) = \frac{R^2H^2}{R^2+H^2}\left(\frac{V^2}{R^2} + \frac{B}{H} - \frac{\beta UV}{R}\right) \tag{60}$$

As seen from Eq. (60), in the limit of a large storm (i.e., $R \gg H$), it is apparent that $\Delta\Phi = BH$, which is identical to Eq. (11) use in section 2. This result is physically expected because a large storm tends to approach the hydrostatic balance. In the limit of $H \gg R$, one has $\Delta\Phi \sim V^2$, which results in the HSD system exactly obtained in K2015. Regardless of the limit of the small or large storm, note that $\Delta\Phi$ will be always of the form $\Delta\Phi \sim BH + V^2 + UV$. Upon substituting Eq. (60) back into Eq. (54), the new system of Eqs. (54)–(57) becomes similar to the MSD system (30)–(32) examined in section 2 above, at least in the nondimensional form as follows:

$$\frac{du}{dt} = p_1v^2 + p_2b + p_3uv, \tag{61}$$

$$\frac{dv}{dt} = -uv - v^2, \tag{62}$$

$$\frac{db}{dt} = bu + su + v + rb, \tag{63}$$

where the new set of coefficients (p_1, p_2, p_3) in Eq. (61) now incorporate the impacts of nonhydrostatic effects, which are different from the values $[p, -(p+1), -1]$ in Eq. (30) of the MSD system.

With the similar functional form for the forcing on the right-hand side of Eqs. (61)–(63) as in the MSD system, it is anticipated that the stability of the MSD system would not drastically change. Indeed, our numerical experiments with the system in Eqs. (61)–(63) do confirm the same stability as in the original MSD system (30)–(32), albeit the critical point is slightly shifted. Thus, the MSD system (30)–(32) is compatible with the HSD system presented in K2015 and explains why the stability properties in the new MSD system presented in this study are similar to those obtained by K2015. In this regard, the strong diagnostic constraint of the continuity equation reveals a surprising fact that the gradient wind balance and the nonhydrostatic equation are consistent with the gradient wind imbalance in the PBL under the hydrostatic approximation.

5. Conclusions

In this study, a low-order model based on the TC basic scales has been presented to study the stability of the MPI equilibrium. Unlike the previous model proposed by K2015 in which the gradient wind balance and neutral stratification were assumed, the modified TC-scale dynamical (MSD) model in this study takes into account both the gradient wind imbalance in the PBL and the atmospheric stratification. Stability analyses of this extended model showed a similar MPI critical point under the WISHE feedback mechanism. Specifically, we established that the MPI critical point in the extended TC-scale model has the same structural stability property as in K2015's model.

Unlike the traditional approach to the MPI equilibrium that is based on either integration of the thermal wind along the eyewall AAM surface or the heat-engine approach (Emanuel 1986, 1988), the MPI equilibrium obtained from the MSD system in this present study is a natural result of the TC internal dynamics under the WISHE feedback. That different approaches and balance approximations could lead to the same MPI point and stability behaviors suggests the unique nature of the MPI equilibrium, whose asymptotic stability can be

reasonably captured by gradient wind balance and hydrostatic balance.

Our analyses of the MPI critical point in the presence of both radiative forcing and tropospheric stratification showed further that the MPI depends more sensitively on the stratification of the atmosphere than on the radiative forcing. For the case of weak radiative forcing, an approximated expression for the MPI as a function of the tropospheric stratification is given by $V_c^2 = V_{\rm MPI}^2(1-s)$, where s is a parameter representing the tropospheric stratification [i.e., $s \sim (\Gamma_d - \Gamma)$]. This is an important finding, as it demonstrates how the MPI equilibrium explicitly depends on the environmental lapse rate Γ beyond the traditional MPI theory. As seen from this new MPI expression, a more stable atmosphere will be less conducive to the TC development and result in a lower MPI limit under the same SST and outflow conditions.

Additional examination of the MSD model revealed also that TC development is inherently characterized by two different time scales. Specifically, there exists a short time scale (<1 h), which is associated with the fast oscillation related to the strong competition between the centrifugal force and the inward pressure gradient. The frequency of this fast oscillation is approximately proportional to the ratio of the MPI limit $V_{\rm MPI}$ over the RMW R. In contrast, the other longer time scale is related to a slower increase of the frictional force with time. Given that the frictional force is proportional to the v^2, it would take a longer time (~1 day) for the frictional force to balance the acceleration due to the inward advection of the absolute angular momentum, thus explaining the existence of a longer time scale in TC development. It is this longer time scale that determines the asymptotic convergence toward the MPI equilibrium. The existence of these two time scales indicates that TC development is not a simple monotonic growth as often assumed in previous studies of TC development but should be characterized by two different time scales.

Similar to the HSD model presented in K2015, the MSD model in this study suffers from a number of weaknesses. First, the MSD model does not include detailed microphysics processes, cloud radiative feedbacks, or the eye dynamics that may change the MPI limit and potentially affect its stability. While the MSD model could allow for the imbalance process in the PBL, the lack of these physical processes prevents the MSD model from describing a number of important features such as supergradient wind, eyewall replacement, the weak subsidence in the TC eye, or how TCs can interact with vertical wind shear. These issues can only be properly addressed using the full-physics model, which is, however, beyond the scope of the TC-scale framework. Our modest goal of this study is to provide different insight into the stability of the MPI equilibrium with different balanced approximations under idealized large-scale conditions. As such, these caveats are unavoidable.

A second shortcoming of the MSD model is related to the unaccounted variations of different length scales such as the change of the PBL depth h, the vertical depth of the troposphere H, or the RMW R. Among several different length scales, the assumption of a fixed RMW R seems to be the least justified, because R is known to contract during TC rapid intensification. It should be noted, however, that this assumption of a fixed RMW is not a serious problem in our analyses of the asymptotic MPI stability, because the scale of the RMW is about 10^4–10^5 m. Our examination of a variation of the RMW between 30 and 100 km captures a small change in all TC-scale analyses. In addition, the RMW contraction is most rapid at the early stage of TC intensification. Very often the contraction ceases at the middle of the intensification and subsequently maintains a nearly constant RMW after a vortex becomes sufficiently strong (Kieu 2012). As such, the assumption of a fixed RMW is not a severe limit in our stability analyses, at least from the asymptotic MPI stability perspective. Of course, this justification of a fixed RMW by no means overcomes the shortcomings of the MSD model due to other unaccounted variations and approximations. In this regard, the applicability of the MSD model should be limited within an idealized framework and further validated using the full-physics models that we plan to follow in a future study.

Acknowledgments. This research was supported by the NOAA HFIP funding (Award NA16NWS4680026), the ONR funding (Grant N000141410143), and the Vice Provost for Research through the Indiana University Faculty Research Support Program. We thank Dr. Shouhong Wang (Indiana University Bloomington) and four anonymous reviewers for their constructive suggestions and comments.

APPENDIX A

Coriolis Effects on the MPI Limit

Inclusion of the Coriolis force in the MSD system results in much more complex analyses of critical points and their related stability. In this appendix, we will show that inclusion of the Coriolis force will not change the stability of the MPI equilibrium. While there are more

technical issues related to the existence of additional critical points and expansion of the basin of attraction, it suffices to present an important result that there is still only one stable critical point in the presence of the Coriolis force, and it is in the neighborhood of the critical points (u_c, v_c, b_c) given by Eq. (33) for the case $f = 0$. In addition, the structural stability of this critical point is not changed. To prove this result, we note that in the nondimensional form, the MSD system with the Coriolis force will have two extra terms in the radial momentum equation and the tangential momentum equation as follows:

$$\dot{u} = pv^2 - (p+1)b - uv + pfv, \tag{A1}$$

$$\dot{v} = -uv - v^2 - fu, \tag{A2}$$

$$\dot{b} = bu + su + v - rb, \tag{A3}$$

where $f = f^*U_c/(\beta V_c^2) \approx 0.05$ is a nondimensional number representing impacts of the Coriolis force and $f^* = 2\Omega\sin(\varphi) \approx 10^{-4}$–$10^{-5}\,\mathrm{s}^{-1}$ is the typical dimensional Coriolis parameter at a given latitude $\varphi \approx 10°\mathrm{N}$. The critical points for system (A1)–(A3) satisfy the following algebraic equations:

$$pv^2 - (p+1)b - uv + pfv = 0, \tag{A4}$$

$$-uv - v^2 - fu = 0, \tag{A5}$$

$$bu + su + v - rb = 0. \tag{A6}$$

Obviously, (0, 0, 0) is a solution of Eqs. (A4)–(A6), and all other critical points v of Eqs. (A4)–(A6) satisfy the following equation:

$$v^4 + av^3 + bv^2 + cv + d = 0, \tag{A7}$$

where coefficients a, b, c, and d are given by

$$a = \frac{2pf}{p+1} + r, \tag{A8}$$

$$b = \frac{2pfr}{p+1} + fr + s - 1 + \frac{pf^2}{p+1}, \tag{A9}$$

$$c = \frac{3prf^2}{p+1} + f(s-2), \tag{A10}$$

$$d = -f^2 + \frac{prf^3}{p+1}. \tag{A11}$$

Note that when $f = 0$, Eqs. (A8)–(A11) are equivalent to

$$v^2 + rv + s - 1 = 0, \tag{A12}$$

and the roots of Eq. (A12) are as follows:

$$v_1 = \frac{-r + \sqrt{r^2 + 4 - 4s}}{2}, \tag{A13}$$

$$v_2 = \frac{-r - \sqrt{r^2 + 4 - 4s}}{2}, \tag{A14}$$

as established in section 3 so that system (A1)–(A3) has three critical points given by

$$\mathbf{x}_0 = (0,0,0), \quad \mathbf{x}_1 = \left(-v_1, v_1, \frac{(1-s)v_1}{r+v_1}\right),$$
$$\mathbf{x}_2 = \left(-v_2, v_2, \frac{(1-s)v_2}{r+v_2}\right), \quad s \neq 1. \tag{A15}$$

Given these critical point for $f = 0$, we show next that Eqs. (A1)–(A3) will have only two real nonzero critical points for $0 < |f| \ll 1$; one is in the δ neighborhood of the $\mathbf{x}_1$, and the other is in the δ neighborhood of the $\mathbf{x}_2$. Denote

$$\mathbf{F}(\mathbf{x}, f) = \begin{bmatrix} pv^2 - (p+1)b - uv + pfv \\ -uv - v^2 - fu \\ bu + su + v - rb \end{bmatrix}, \quad \mathbf{x} = \begin{pmatrix} u \\ v \\ b \end{pmatrix}. \tag{A16}$$

Let $\mathbf{x} = \mathbf{y} + \mathbf{x}_i$ ($i = 1$ or 2), where $\mathbf{y}$ is a small perturbation around the critical point $\mathbf{x_i}$, and

$$\mathbf{M} = \begin{bmatrix} -v_i & 2pv_i + v_i + pf & -p-1 \\ -v_i - f & -v_i & 0 \\ \dfrac{(1-s)v_i}{r+v_i} + s & 1 & -v_c - r \end{bmatrix}, \tag{A17}$$

then the Jacobian of Eqs. (A1)–(A3) evaluated at any critical point $\mathbf{x}_i$ can be approximated as an expansion in terms of the Coriolis parameter f as follows:

$$\mathbf{G}(\mathbf{x}, f) \equiv \mathbf{F}(\mathbf{x}_i + \mathbf{y}, f) = \mathbf{M}\mathbf{y}^{\mathrm{T}} + \mathbf{h}(\mathbf{y}), \tag{A18}$$

$$\mathbf{h}(\mathbf{y}) = \begin{pmatrix} Py_2^2 - y_1y_2 + pfv_i \\ -y_1y_2 - y_2^2 + fv_i \\ y_3y_1 \end{pmatrix}. \tag{A19}$$

Furthermore, we have

$$\left.\frac{\partial \mathbf{G}(\mathbf{y}, f)}{\partial \mathbf{y}}\right|_{(\mathbf{y},f)=(0,0,0,0)} = \begin{bmatrix} -v_i & 2pv_i + v_i & -p-1 \\ -v_i & -v_i & 0 \\ \dfrac{(1-s)v_i}{r+v_i} + s & 1 & -v_i - r \end{bmatrix}, \tag{A20}$$

and

$$\det\left[\left.\frac{\partial \mathbf{G}(\mathbf{y},f)}{\partial \mathbf{y}}\right|_{(\mathbf{y},f)=(0,0,0,0)}\right], \tag{A21}$$

$$=\begin{vmatrix} -v_i & 2pv_i+v_i & -p-1 \\ -v_i & -v_i & 0 \\ \dfrac{(1-s)v_i}{r+v_i}+s & 1 & -v_i-r \end{vmatrix}, \tag{A22}$$

$$=(p+1)(1-s)\frac{rv_i-2(1-s)}{r+v_i}\neq 0 \quad (s\neq 1). \tag{A23}$$

By the implicit function theorem, there exists a positive number $1\gg\lambda_0>0$ such that for any $|y|<\lambda_0$, Eqs. (A4)–(A6) have two zeros given by

$$\mathbf{x}_{fi}=\mathbf{x}_i+\boldsymbol{\varphi}_i(f), \quad \boldsymbol{\varphi}_i(0)=0, \quad i=1,2. \tag{A24}$$

Hence, for $0<|f|<\delta\ll 1$, the system (A4)–(A6) has two critical points, which are in the small neighborhood of points $\mathbf{x}_1$ and $\mathbf{x}_2$, respectively. Following the same analyses, it is possible to show further that the other two roots of Eq. (A7) are complex as the set of parameters (r, s, f) are near the point (0, 1, 0) but real when (r, s, f) are near the point (0, 0, 0); both are unstable and will not be hereinafter examined further.

To finally confirm the stability of the critical points $\mathbf{x}_1$ and $\mathbf{x}_2$ of the system (A1)–(A3), let $\mathbf{x}_c=(v_c, w_c, b_c)$ be any critical points, the Jacobi matrix $\mathbf{F}$ at $\mathbf{x}_c$ is as follows:

$$\left.\frac{\partial \mathbf{F}(\mathbf{x})}{\partial \mathbf{y}}\right|_{(\mathbf{x}_c)=(v_c,w_c,b_c)}=\begin{pmatrix} -v_c & 2pv_c-u_c+pf & -p-1 \\ -v_c-f & -u_c-2v_c & 0 \\ b_c+s & 1 & u_c-r \end{pmatrix}, \tag{A25}$$

Direct calculation of the determinant of Eq. (A25) yields the following characteristic equation of matrix $\mathbf{F}$:

$$\lambda^3+A\lambda^2+B\lambda+C=0, \tag{A26}$$

where

$$A(\mathbf{x}_c,p,r,s,f)=3v_c+r, \tag{A27}$$

$$\begin{aligned} B(\mathbf{x}_c,p,r,s,f)&=2(p+1)v_c^2+3pfv_c-fu_c \\ &\quad-(u_c-r)(3v_c+u_c) \\ &\quad+(p+1)(b_c+s)+pf^2, \end{aligned} \tag{A28}$$

$$\begin{aligned} C(\mathbf{x}_c,p,r,s,f)&=(p+1)(b_cu_c+2b_cv_c+su_c+2sv_c)-(u_c-r)(2v_c^2+2pv_c^2+3pfv_c-fu_c) \\ &\quad-(p+1)(v_c+f)-pf(fu_c-rf). \end{aligned} \tag{A29}$$

For the case of $f=0$, one recovers the coefficients A, B, and C as in section 2a as follows:

$$A(\mathbf{x}_i,p,r,s,0)=3v_i+r, \tag{A30}$$

$$B(\mathbf{x}_i,p,r,s,0)=2(p+1)v_i^2+2v_i(v_i+r)+(p+1)\frac{v_i+rs}{r+v_i}, \tag{A31}$$

$$\begin{aligned} C(\mathbf{x}_c,p,r,s,f)&=(p+1)(b_iv_i+sv_i)+(v_i+r)2(p+1)v_i^2 \\ &\quad-(p+1)v_i, \end{aligned} \tag{A32}$$

Obviously,

$$A(\mathbf{x}_2,p,r,s,0)<0, \tag{A33}$$

which means Eq. (A26) has at least one positive root (i.e., $\mathbf{x}_2$) that is unstable as expected. For the critical point $\mathbf{x}_1$, it is stable if and only if

$$A(\mathbf{x}_1,p,r,s,0)>0, \quad C(\mathbf{x}_1,p,r,s,0)>0, \tag{A34}$$

$$A(\mathbf{x}_1,p,r,s,0)B(\mathbf{x}_1,p,r,s,0)-C(\mathbf{x}_1,p,r,s,0)>0. \tag{A35}$$

With the exact expression in Eq. (A14), we get

$$A(\mathbf{x}_i,p,r,s,0)=3\sqrt{\frac{r^2}{4}+1-s}-\frac{r}{2}>0, \tag{A36}$$

$$B(\mathbf{x}_i,p,r,s,0)=(p+1)\left(\frac{3v_1^2-2sv_1^2+rsv_1}{1-s}+\frac{2-2s}{p+1}\right)>0, \tag{A37}$$

$$C(\mathbf{x}_1,p,r,s,f)=(p+1)(v_1^3+v_1-sv_1)>0, \tag{A38}$$

and

$$A(\mathbf{x}_i,p,r,s,0)B(\mathbf{x}_i,p,r,s,0)-C(\mathbf{x}_i,p,r,s,0), \tag{A39}$$

$$=(p+1)\left[\left(3\sqrt{\frac{r^2}{4}+1-s}-\frac{r}{2}\right)\right.$$

$$\times\left(\frac{3v_1^2-2sv_1^2+rsv_1}{1-s}+\frac{2-2s}{p+1}\right), \quad \text{(A40)}$$

$$\left.-(p+1)(v_1^3+v_1-sv_1)\right], \quad \text{(A41)}$$

$$\geq(p+1)[(3v_1+r)2v_1^2-v_1^3-v_1-sv_1]>0. \quad \text{(A42)}$$

All conditions for the existence of eigenvalues with negative real parts are thus satisfied, and $\mathbf{x}_1$ is stable. Note further that Eqs. (A36)–(A42) and the eigenvalue of matrix (A25) are continuously dependent on f and the nonzero critical points $\mathbf{x}_{1,2}$ are hyperbolic. Hence, based on the Hartman–Grobman theorem, those nonzero critical points are locally structural stability. As a result, the stability of the MPI critical point is again established in a more general case with the Coriolis force as discussed in the main text. More subtle impacts of the Coriolis on TC development can be found in Kieu and Wang (2017).

APPENDIX B

Eigenvector Analyses at the MPI Limit

As a demonstration of the linear analysis for the Jacobian matrix evaluated at the critical point $\mathbf{x}_c$ in the main text, we consider first a set of parameters $(p, r, s) = (10, 0, 0)$ around which the stability proof presented in section 3b is approximated. Using a numerical solver, the approximated eigenvalues for Eq. (38) are given by

$$\lambda_1 = -1.1712 + 5.6646i, \quad \lambda_2 = -1.1712 - 5.6646i,$$
$$\lambda_3 = -0.6575,$$

which correspond to the following eigenvectors:

$$\mathbf{e}_1 = \begin{pmatrix} -0.9697 \\ -0.0052 - 0.1710i \\ -0.0250 + 0.1728i \end{pmatrix}, \quad \text{(B1)}$$

$$\mathbf{e}_2 = \begin{pmatrix} -0.9697 \\ -0.0052 + 0.1710i \\ -0.0250 - 0.1728i \end{pmatrix}, \quad \text{(B2)}$$

$$\mathbf{e}_3 = \begin{pmatrix} -0.1563 \\ 0.4563 \\ 0.8760 \end{pmatrix}. \quad \text{(B3)}$$

Consider next another set of parameters $(p, r, s) = (10, 0.1, 0.1)$ that is in sufficiently close neighborhood of $(p, r, s) = (10, 0, 0)$. Direct calculation of the eigenvalues and eigenvectors for the linearized Jacobian matrix again gives

$$\lambda_1' = -1.1010 + 5.2059i, \quad \lambda_2' = -1.1010 - 5.2059i,$$
$$\lambda_3' = -0.5979,$$

and the corresponding eigenvectors are

$$\mathbf{e}_1' = \begin{pmatrix} -0.9704 \\ -0.0065 - 0.1675i \\ -0.0289 + 0.1714i \end{pmatrix}, \quad \text{(B4)}$$

$$\mathbf{e}_2' = \begin{pmatrix} -0.9704 \\ -0.0065 + 0.1675i \\ -0.0289 - 0.1714i \end{pmatrix}, \quad \text{(B5)}$$

$$\mathbf{e}_3' = \begin{pmatrix} -0.1658 \\ 0.4941 \\ 0.8535 \end{pmatrix}. \quad \text{(B6)}$$

A quick comparison of the eigenvalues and eigenvectors between these two sets of parameters confirms that these values are very close, thus indicating that the proof of the stability based on the Taylor expansion presented in section 3b is correct.

REFERENCES

Abramowitz, M., and I. A. Stegun, 1972: *Handbook of Mathematical Functions with Formulas, Graphs, and Mathematical Tables.* Dover, 1046 pp.

Alligood, K. T., T. Sauer, and J. Yorke, 1996: *An Introduction to Dynamical Systems.* Springer-Verlag, 603 pp.

Anthes, R. A., 1974: The dynamics and energetics of mature tropical cyclones. *Rev. Geophys.*, **12**, 495–522, doi:10.1029/RG012i003p00495.

Brown, B. R., and G. J. Hakim, 2013: Variability and predictability of a three-dimensional hurricane in statistical equilibrium. *J. Atmos. Sci.*, **70**, 1806–1820, doi:10.1175/JAS-D-12-0112.1.

Bryan, G. H., and R. Rotunno, 2009: The maximum intensity of tropical cyclones in axisymmetric numerical model simulations. *Mon. Wea. Rev.*, **137**, 1770–1789, doi:10.1175/2008MWR2709.1.

Charney, J. G., and A. Eliassen, 1964: On the growth of the hurricane depression. *J. Atmos. Sci.*, **21**, 68–75, doi:10.1175/1520-0469(1964)021<0068:OTGOTH>2.0.CO;2.

Emanuel, K. A., 1986: An air–sea interaction theory for tropical cyclones. Part I: Steady-state maintenance. *J. Atmos. Sci.*, **43**, 585–605, doi:10.1175/1520-0469(1986)043<0585:AASITF>2.0.CO;2.

——, 1988: The maximum intensity of hurricanes. *J. Atmos. Sci.*, **45**, 1143–1155, doi:10.1175/1520-0469(1988)045<1143:TMIOH>2.0.CO;2.

——, 2000: A statistical analysis of tropical cyclone intensity. *Mon. Wea. Rev.*, **128**, 1139–1152, doi:10.1175/1520-0493(2000)128<1139:ASAOTC>2.0.CO;2.

——, and R. Rotunno, 2011: Self-stratification of tropical cyclone outflow. Part I: Implications for storm structure. *J. Atmos. Sci.*, **68**, 2236–2249, doi:10.1175/JAS-D-10-05024.1.

Garner, S., 2015: The relationship between hurricane potential intensity and CAPE. *J. Atmos. Sci.*, **72**, 141–163, doi:10.1175/JAS-D-14-0008.1.

Hack, J. J., and W. H. Schubert, 1986: Nonlinear response of atmospheric vortices to heating by organized cumulus

convection. *J. Atmos. Sci.*, **43**, 1559–1573, doi:10.1175/1520-0469(1986)043<1559:NROAVT>2.0.CO;2.

Hakim, G. J., 2011: The mean state of axisymmetric hurricanes in statistical equilibrium. *J. Atmos. Sci.*, **68**, 1364–1376, doi:10.1175/2010JAS3644.1.

——, 2013: The variability and predictability of axisymmetric hurricanes in statistical equilibrium. *J. Atmos. Sci.*, **70**, 993–1005, doi:10.1175/JAS-D-12-0188.1.

Hill, K. A., and G. M. Lackmann, 2011: The impact of future climate change on TC intensity and structure: A downscaling approach. *J. Climate*, **24**, 4644–4661, doi:10.1175/2011JCLI3761.1.

Kieu, C. Q., 2012: An investigation into the contraction of the hurricane radius of maximum wind. *Meteor. Atmos. Phys.*, **115**, 47–56, doi:10.1007/s00703-011-0171-7.

——, 2015: Hurricane maximum potential intensity equilibrium. *Quart. J. Roy. Meteor. Soc.*, **141**, 2471–2480, doi:10.1002/qj.2556.

——, 2016: Retrograde waves in tropical cyclone inner-core. *Tellus*, **68A**, 31402, doi:10.3402/tellusa.v68.31402.

——, and Z. Moon, 2016: Hurricane intensity predictability. *Bull. Amer. Meteor. Soc.*, **97**, 1847–1857, doi:10.1175/BAMS-D-15-00168.1.

——, and Q. Wang, 2017: On the scale dynamics of tropical cyclone intensity. *Discrete Contin. Dyn. Syst.*, **22B**, doi:10.3934/dcdsb.2017196, in press.

——, H. Chen, and D. L. Zhang, 2010: An examination of the pressure–wind relationship for intense tropical cyclones. *Wea. Forecasting*, **25**, 895–907, doi:10.1175/2010WAF2222344.1.

Liu, Y., D.-L. Zhang, and M. K. Yau, 1999: A multiscale numerical study of Hurricane Andrew (1992). Part II: Kinematics and inner-core structures. *Mon. Wea. Rev.*, **127**, 2597–2616, doi:10.1175/1520-0493(1999)127<2597:AMNSOH>2.0.CO;2.

Ma, T., and S. Wang, 2011: Phase transitions for Belousov–Zhabotinsky reactions. *Math. Methods Appl. Sci.*, **34**, 1381–1397, doi:10.1002/mma.1446.

Montgomery, M. T., and R. K. Smith, 2014: Paradigms for tropical-cyclone intensification. *Aust. Meteor. Ocean.*, **64**, 37–66, doi:10.22499/2.6401.005.

Ogura, Y., and N. A. Phillips, 1962: Scale analysis of deep and shallow convection in the atmosphere. *J. Atmos. Sci.*, **19**, 173–179, doi:10.1175/1520-0469(1962)019<0173:SAODAS>2.0.CO;2.

Ooyama, K., 1969: Numerical simulation of the life cycle of tropical cyclones. *J. Atmos. Sci.*, **26**, 3–40, doi:10.1175/1520-0469(1969)026<0003:NSOTLC>2.0.CO;2.

Palmer, T. N., 1993: Extended-range atmospheric prediction and the Lorenz model. *Bull. Amer. Meteor. Soc.*, **74**, 49–65, doi:10.1175/1520-0477(1993)074<0049:ERAPAT>2.0.CO;2.

Rotunno, R., and K. A. Emanuel, 1987: An air–sea interaction theory for tropical cyclones. Part II: Evolutionary study using a nonhydrostatic axisymmetric numerical model. *J. Atmos. Sci.*, **44**, 542–561, doi:10.1175/1520-0469(1987)044<0542:AAITFT>2.0.CO;2.

Schönemann, D., and T. Frisius, 2012: Dynamical system analysis of a low-order tropical cyclone model. *Tellus*, **64A**, 15817, doi:10.3402/tellusa.v64i0.15817.

Schubert, W. H., C. M. Rozoff, J. L. Vigh, B. D. McNoldy, and J. P. Kossin, 2007: On the distribution of subsidence in the hurricane eye. *Quart. J. Roy. Meteor. Soc.*, **133**, 595–605, doi:10.1002/qj.49.

Shen, W., R. E. Tuleya, and I. Ginis, 2000: A sensitivity study of the thermodynamic environment on GFDL model hurricane intensity: Implications for global warming. *J. Climate*, **13**, 109–121, doi:10.1175/1520-0442(2000)013<0109:ASSOTT>2.0.CO;2.

Smith, R. K., and M. T. Montgomery, 2015: Toward clarity on understanding tropical cyclone intensification. *J. Atmos. Sci.*, **72**, 3020–3031, doi:10.1175/JAS-D-15-0017.1.

——, G. Kilroy, and M. T. Montgomery, 2015: Why do model tropical cyclones intensify more rapidly at low latitudes? *J. Atmos. Sci.*, **72**, 1783–1804, doi:10.1175/JAS-D-14-0044.1.

Tuleya, R. E., M. Bender, T. R. Knutson, J. J. Sirutis, B. Thomas, and I. Ginis, 2016: Impact of upper-tropospheric temperature anomalies and vertical wind shear on tropical cyclone evolution using an idealized version of the operational GFDL hurricane model. *J. Atmos. Sci.*, **73**, 3803–3820, doi:10.1175/JAS-D-16-0045.1.

Wilhelmson, R., and Y. Ogura, 1972: The pressure perturbation and the numerical modeling of a cloud. *J. Atmos. Sci.*, **29**, 1295–1307, doi:10.1175/1520-0469(1972)029<1295:TPPATN>2.0.CO;2.

Willoughby, H. E., 1979: Forced secondary circulations in hurricanes. *J. Geophys. Res.*, **84**, 3173–3183, doi:10.1029/JC084iC06p03173.

——, 1990: Gradient balance in tropical cyclones. *J. Atmos. Sci.*, **47**, 265–274, doi:10.1175/1520-0469(1990)047<0265:GBITC>2.0.CO;2.

Yanai, M., 1964: Formation of tropical cyclones. *Rev. Geophys.*, **2**, 367–414, doi:10.1029/RG002i002p00367.